Measurements of Melt Pool Geometry and Cooling Rates of Individual Laser Traces on IN625 Bare Plates

Brandon Lane[1] · Jarred Heigel[1] · Richard Ricker[3] · Ivan Zhirnov[2] · Vladimir Khromschenko[2] · Jordan Weaver[1] · Thien Phan[1] · Mark Stoudt[3] · Sergey Mekhontsev[2] · Lyle Levine[3]

Abstract

The complex physical nature of the laser powder bed fusion (LPBF) process warrants use of multiphysics computational simulations to predict or design optimal operating parameters or resultant part qualities such as microstructure or defect concentration. Many of these simulations rely on tuning based on characteristics of the laser-induced melt pool, such as the melt pool geometry (length, width, and depth). Additionally, many of numerous interacting variables that make the LPBF process so complex can be reduced and controlled by performing simple, single-track experiments on bare (no powder) substrates, yet still produce important and applicable physical results. The 2018 Additive Manufacturing Benchmark (AM Bench) tests and measurements were designed for this application. This paper describes the experiment design for the tests conducted using LPBF on bare metal surfaces, and the measurement results for the melt pool geometry and melt pool cooling rate performed on two LPBF systems. Several factors, such as accurate laser spot size, were determined after the 2018 AM Bench conference, with results of those additional tests reported here.

Keywords Laser powder bed fusion · Selective laser melting · Thermography · Melt pool length · Cooling rate

Introduction

This paper describes the experiment design and measurement results of melt pool geometry (length, width, and depth), as well as cooling rate measurements for comparison to numerical process simulations pertaining to bare metal scans. These tests were part of several types of benchmark tests and measurements for the 2018 Additive Manufacturing Benchmark Tests (AM Bench) and given the indicator AMB2018-02 on the AM-Bench website [1]. Single-track experiments were chosen to reduce the number of experiment variables and ensure broad utility among modelers. Additionally, these tests are conducted on bare substrates without powder to further reduce the number of variables (e.g., powder size distribution or powder layer height) and reduce potential variability due to secondary physical phenomena (e.g., powder denudation or track instability), though it has been shown that melt pools formed on bare plate and single layers of powder share similar lengths and cooling rates [2]. The experiments were conducted on two different LPBF systems; the Additive Manufacturing Metrology Testbed (AMMT) [3] and an EOS M270[1] commercial build machine (CBM).

Experiment Setup

Sample Preparation and Test Parameters

Nickel-based superalloy 625 (IN625) substrates are used in this study. They measure 24.5 mm × 4.5 mm and 3.2 mm

---

✉ Brandon Lane
brandon.lane@nist.gov

1 Engineering Laboratory, NIST, Gaithersburg, MD, USA

2 Physical Measurement Laboratory, NIST, Gaithersburg, MD, USA

3 Materials Measurement Laboratory, NIST, Gaithersburg, MD, USA

1 Certain commercial equipment, instruments, or materials are identified in this paper in order to specify the experimental procedure adequately. Such identification is not intended to imply recommendation or endorsement by the National Institute of Standards and Technology, nor is it intended to imply that the materials or equipment identified are necessarily the best available for the purpose.
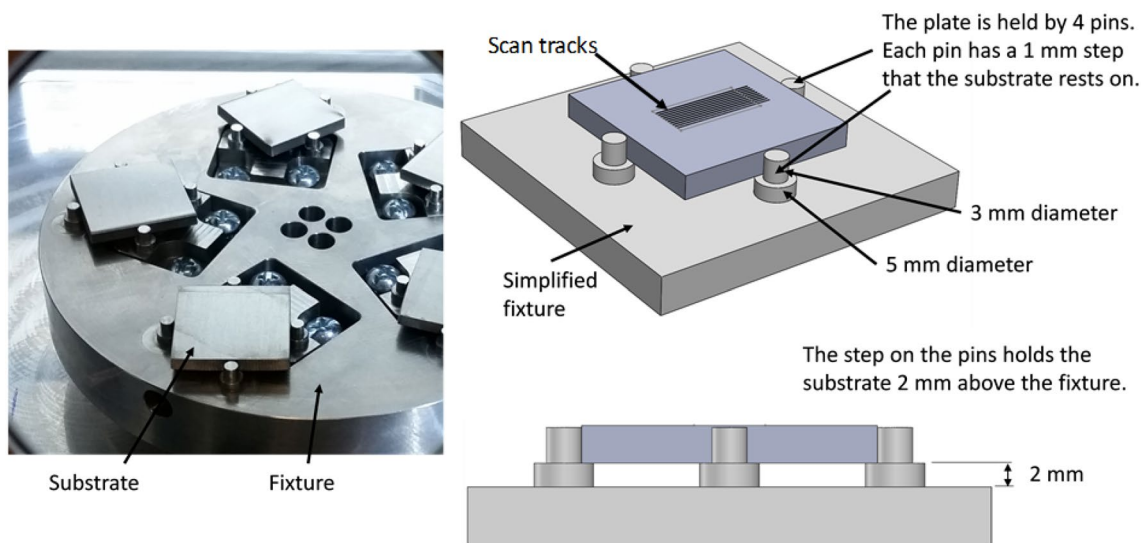
Fig. 1 Illustration of the substrate as it is held in the fixture inside the CBM. AMMT had a similar holding system
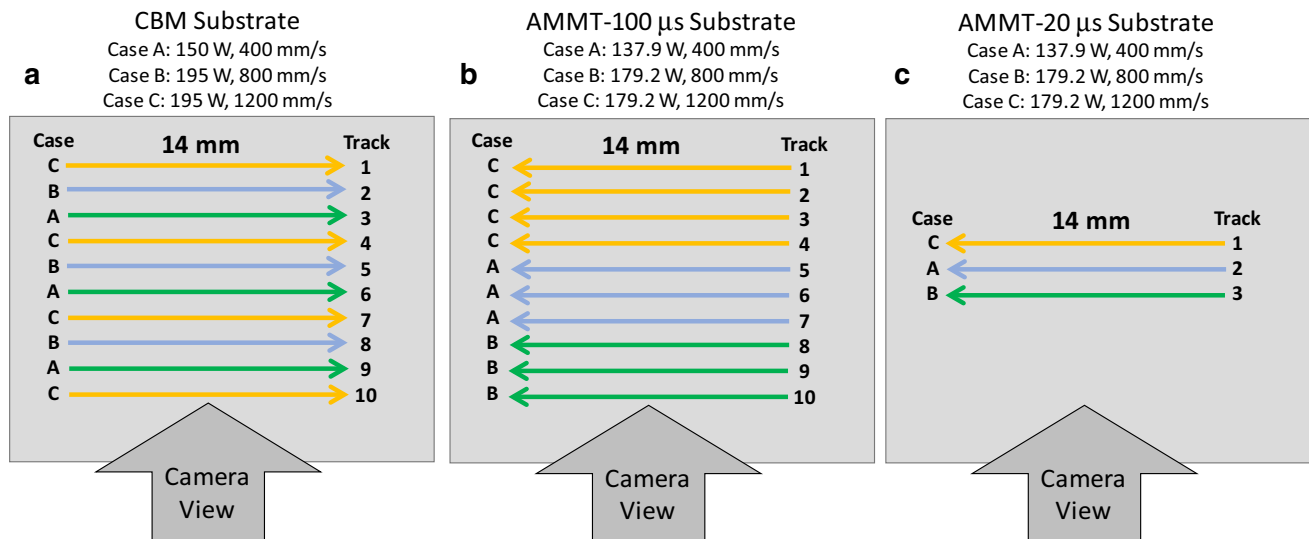

Fig. 2 Track numbering and layout for each set of measurements: **a** CBM, **b** AMMT-100 µs, and **c** AMMT-20 µs. Laser power values indicated are the applied laser power

thick. The substrate surface is prepared with 320 grit random orientation polishing to create a flat, optically diffuse surface with surface features much smaller than the melt pool scale (approximately 10's of µm). Substrates were held in the AMMT and CBM systems by four pins in a fixture. Figure 1 presents an illustration of the fixturing method. This setup was introduced in prior work [4] and designed to ensure minimal contact is made on the substrate, which minimizes conductive heat loss. The fixture and pins are made of aluminum alloy.

Surface roughness of the substrates was measured using laser confocal microscope on three sample areas between the laser scan tracks (approximately 0.3 mm × 1.5 mm, avoiding any scan track topography). Arithmetic mean height areal parameter values ranged from Sa = 0.44–0.53 µm and root mean square height parameter values from Sq = 0.64–0.73 µm.

Scan parameters (laser power and scan speed) are identified by 'Case,' with the following parameter values: Case A laser power and speed are 150 W and 400 mm/s, Case B are 195 W and 800 mm/s, and Case C are 195 W and

Table 1 Machine parameters for the CBM and AMMT systems

	CBM	AMMT
Laser spot size	D4σ diameter = 100 μm FWHM = 59 μm	D4σ diameter = 170 μm FWHM = 100 μm
Inert gas	Nitrogen	Argon
Oxygen level	≈ 0.5%	< 0.08%

1200 mm/s. Figure 2 shows the track numbering and scan parameter case. Initial AMMT thermal imaging was collected at an integration time of 100 μs (here referred to as AMMT-100 μs). Due to the potential effect of motion blur on the 100 μs thermal images described in "Melt Pool Imaging Thermography Systems" section, a second, limited set of tests were conducted at an integration time of 20 μs (AMMT-20 μs) and compared to the AMMT-100 μs scans to ensure that they were executed under nominally similar conditions.

Laser spot size is set through different mechanisms on the CBM and AMMT. The CBM uses an f-theta lens to create a flat scanning field and an adjustable defocusing lens after the laser collimator to adjust spot size. The AMMT uses a dynamic linear translating z-lens (LTZ) to perform a flat-field correction [3]. This LTZ is mounted and aligned on a second linear stage, which adjusts the static laser focus position and spot size. CBM spot size was presumed to be set based on the manufacturers specifications, and AMMT spot size was measured in situ by attenuating the laser beam after the laser collimator and directly scanning on a charge-coupled device (CCD) array. For the AMMT, 4-sigma diameter (D4σ) was 170 μm (full-width half max (FWHM) of 100 μm) and

the CBM laser spot (D4σ) was 100 μm (FWHM of 59 μm). Spot size and additional machine parameters pertinent to the conditions inside the build chamber are provided in Table 1.

Melt Pool Imaging Thermography Systems

The thermography setup for in situ measurements on the CBM and AMMT varied in several significant ways. However, both systems incorporate a staring configuration that views the melt pool as it scans through the camera field of view. Also, the essential method for calibration, measurement, and analysis of the resulting melt pool images proceeded using similar methods. Figure 3 shows both thermography experiment setups, with description of pertinent components. Table 2 provides a comparison of pertinent technical parameters for both imaging systems.

Since the cameras view their respective surfaces at an angle, the projected pixel size on the build surface (or instantaneous field of view, iFoV) is different in the horizontal and vertical direction in camera image. That is, while each of the camera pixels are square, the true dimensions on the build surface are different in the horizontal and vertical directions. Equivalent iFoV in the vertical image direction is scaled by $r/\cos(\theta)$, with r being the horizontal scale in μm per pixel, and θ being the viewing angle the camera makes with respect to the build surface normal.

The CBM camera is calibrated using a commercial spherical cavity, variable temperature blackbody source, with a circular foil aperture slightly larger than the field of view to avoid stray light which can erroneously increase the signal. The AMMT camera is calibrated using a custom, light emitting diode (LED)-driven integrating sphere, with interchangeable apertures. Both have calibrations tied to the
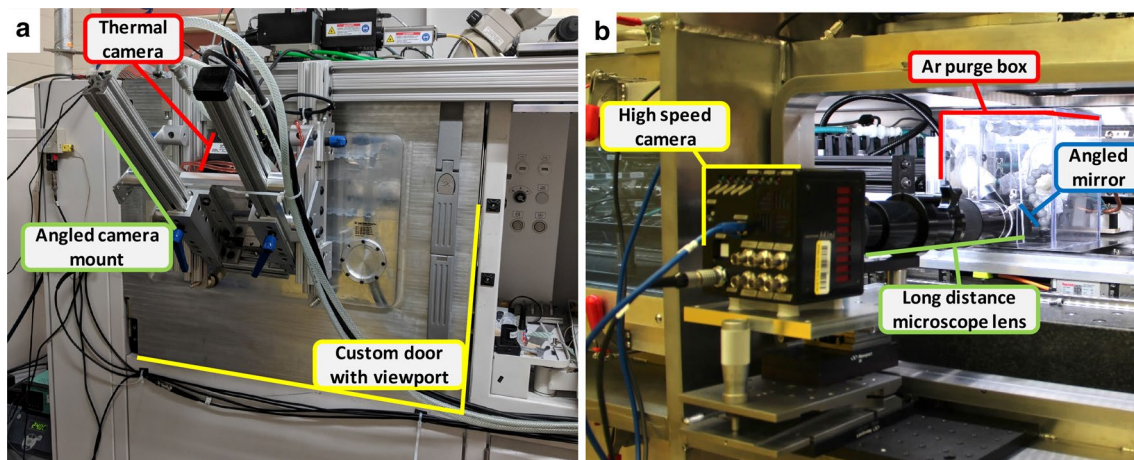

Fig. 3 Thermography setup for each machine: **a** CBM, using a mounting bracket to angle the camera and look through a custom door with viewport, **b** AMMT, using a long distance microscope and angled first-surface mirror mounted in an argon purge box

Table 2 Infrared thermography specifications for the CBM and AMMT systems

	CBM	AMMT
Imager type	Cooled, extended range indium antimonide (InSb)	High-speed Si-based complimentary metal oxide semiconductor (CMOS)
Lens type	50 mm short-wave infrared (SWIR) lens on 12.5 mm extension.	Long-distance microscope (visible spectrum) with attached mirror.
Optical filter bandwidth	1350 nm to 1600 nm	850 nm ± 20 nm
Integration time	40 µs	20 µs or 98 µs
Digital dynamic range	14-bit Saturates at ≈ 12 000 digital levels (DL)	12-bit (0–4095 DL)
Radiant temperature calibration range (at integration time)	500–1050 °C (40 µs)	1000–1650 °C (20 µs) 900–1350 °C (100 µs)
Frame rate	1800/s	10 000/s
Window size	360 pixels × 128 pixels	1024 pixels × 672 pixels
Field of view (FoV)	12.96 mm × 6.82 mm	3.36 mm × 2.20 mm
Detector pixel pitch	12 µm	20 µm
Magnification	0.33x	6x
Instantaneous FoV (iFoV) per pixel	36 µm (horizontal)	3.28 µm (horizontal)
Viewing angle	46.3° from surface normal (43.7° from surface)	24° from surface normal (66° from surface)
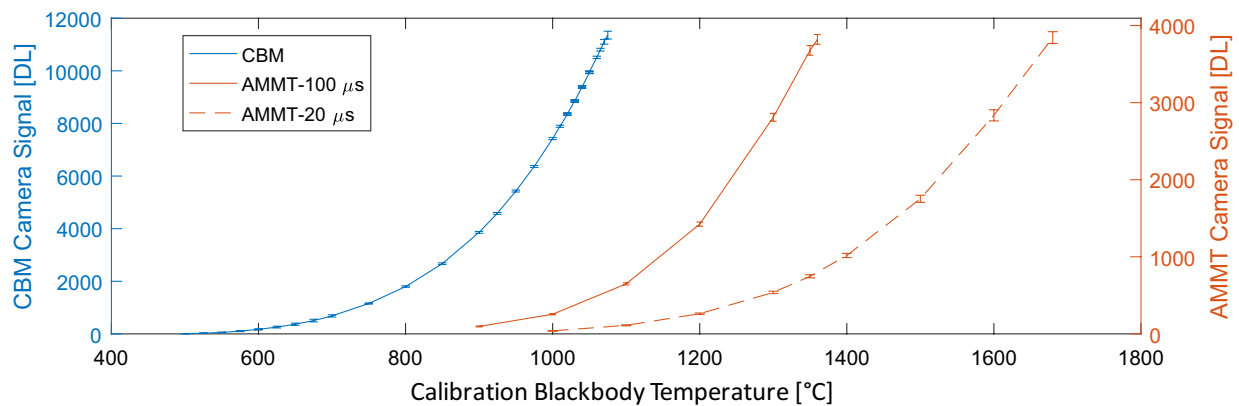
Fig. 4 Thermal calibration points (with linear interpolated lines for clarity) for the CBM and AMMT thermal cameras. Error bars indicate ± 1σ standard deviation

primary standards at NIST. Figure 4 shows the calibration ranges for each of the three samples shown in Fig. 2.

Note that the calibration ranges shown in Fig. 4 do not equate to the true measurable temperature ranges. Since the emitance of the physical surface shifts the measurable range of the true temperature [5], each of the calibration ranges indicated in Fig. 4 does in fact enable observation of the melt pool solidification boundary assumed to be 1290 °C in this paper. The calibration procedure essentially maps digital signals measured by the camera (S_{meas}) to the set point temperature of the calibration blackbody source (T_{bb}), by fitting a nonlinear function F to $S_{meas} = F(T_{bb})$. The Sakuma–Hattori equation [6] is used and described in the next section and closely approximates a spectrally integrated Planckian radiation function, but is invertible in closed form. The contribution of the calibration on measurement uncertainty is discussed in "Measurement Uncertainty" section.

AMMT-100 µs thermal images were collected at 8-bit digital dynamic range (256 DL), whereas the 20 µs thermal imaging (AMMT-20 µs) was collected at 12-bit digital

dynamic range (4096 DL). Thermal calibrations for the AMMT camera were conducted at 12-bit dynamic range setting; therefore, the AMMT-100 μs data had to be upconverted by multiplying the signal value by $2^4 = 16$. The contribution of the digital sampling and digital upconversion AMMT-100 μs to measurement uncertainty is discussed in "Measurement Uncertainty" section. CBM images were collected at 14-bit digital dynamic range (16 384 DL).

Calculation of Melt Pool Length and Cooling Rate

Once thermal images of the melt pool are collected, several processing steps are conducted to convert the camera signal to a temperature that corresponds to the solidification temperature and measure the melt pool length and cooling rate from the profile line taken from the center of the melt pool. First, this section will provide some detail on the difference between radiance temperature (or, apparent temperature), true temperature, and emissivity to provide background on how the line profile data are obtained. Similar publications from the authors provide more detail [4, 5]. In addition, description of the image analysis for extracting melt pool length is provided.

The relationship between measured signal from the camera (S_{meas}), measured in DL, radiance temperature (T_{rad}), true temperature (T_{true}), and emissivity (ε), is defined by the measurement equation:

$$S_{meas} = F(T_{rad}) = \varepsilon F(T_{true}). \tag{1}$$

Radiance temperature is equivalent to a true temperature if $\varepsilon = 1$ (which is approximated when conducting a thermal calibration of the camera against a blackbody calibration source). F is the Sakuma–Hattori calibration function as mentioned before, which relates measured signal [DL] to radiance temperature [°C] or [K]. Often, a $(1 - \varepsilon)$ term representing reflected ambient temperature sources is added to the measurement equation [5]. However, this factor has minimal consequences to measurement of temperatures vastly higher than the ambient surroundings, such as in LPBF melt pool thermographic measurements. The Sakuma–Hattori equation and its inverse are is given in Eqs. (2) and (3):

$$F(T) = \frac{C}{\exp\left(\frac{c_2}{AT+B}\right) - 1} \tag{2}$$

$$F^{-1}(S) = \frac{c_2}{A \ln\left(\frac{C}{S} + 1\right)} - \frac{B}{A}. \tag{3}$$

The term c_2 is the second radiation constant (14,388 μm/K), and the coefficients A, B, and C are fit coefficients determined through least-squares regression.

For thermographic measurements of laser-induced melt pools, a solidification boundary of the melt pool (freezing point) may be distinguished by a discontinuity or inflection point in the temperature versus time ($T(t)$) data or temperature versus length ($T(x)$) profile, assuming laser scan speed is constant. This freezing point is identified by the minimum of the second derivative of $T(x)$, as demonstrated in [4]. This definition follows similar methods used in fixed-point thermometry, in which the solidification point is defined as the inflection point between the solidus and liquidus regions of a melting curve [7].

If the freezing point (nominally the solidus) temperature is known or well approximated, the effective emittance of that point can be extracted from Eq. (1) using Eq. (4) as mentioned in the AMB2018-02 test description [1]. We assume this value, T_{freeze}, is 1290 °C for IN625.

$$\varepsilon_{freeze} = \frac{S_{meas}}{F(T_{freeze})}. \tag{4}$$

Although 1290 °C is an assumed value, it will be shown that this has minimal effect on the melt pool length measurement but does affect the cooling rate measurement. In reality, the solidification temperature is likely affected by undercooling due to the high cooling rates and nonequilibrium solidification [8].

Once calculated, ε_{freeze} can then be used to convert the measured camera signal or radiance temperature in Eq. (1) into 'true' temperature using Eq. (5). Essentially, this scales the measured radiance temperature field (nonlinearly) such that the detected solidification boundary in the thermal images equates to the assumed solidification temperature of 1290 °C. Although this is valid for the solidification point, it is assumed that ε_{freeze} is applicable at temperatures above and below the solidification point, or over the range that cooling rate is measured.

$$T_{true} = F^{-1}\left(\frac{S_{meas}}{\varepsilon_{freeze}}\right). \tag{5}$$

Laser scans for experiments described here are essentially horizontal within the field of view of the camera; therefore, melt pool temperature profiles may be extracted by selecting a horizontal row of pixels at the melt pool center. In the case of non-horizontal scans (not described in this paper), this method is inadequate; therefore, we developed a more universal algorithm for extracting the melt pool temperature profile along its length.

First, an approximate melt pool shape is determined by locating an approximate solidification boundary. The principle axis of this shape, determined from the second central moment, then defines the profile line $T(x)$ along which further melt pool length and cooling rates are calculated. The following algorithm is used to define melt pool
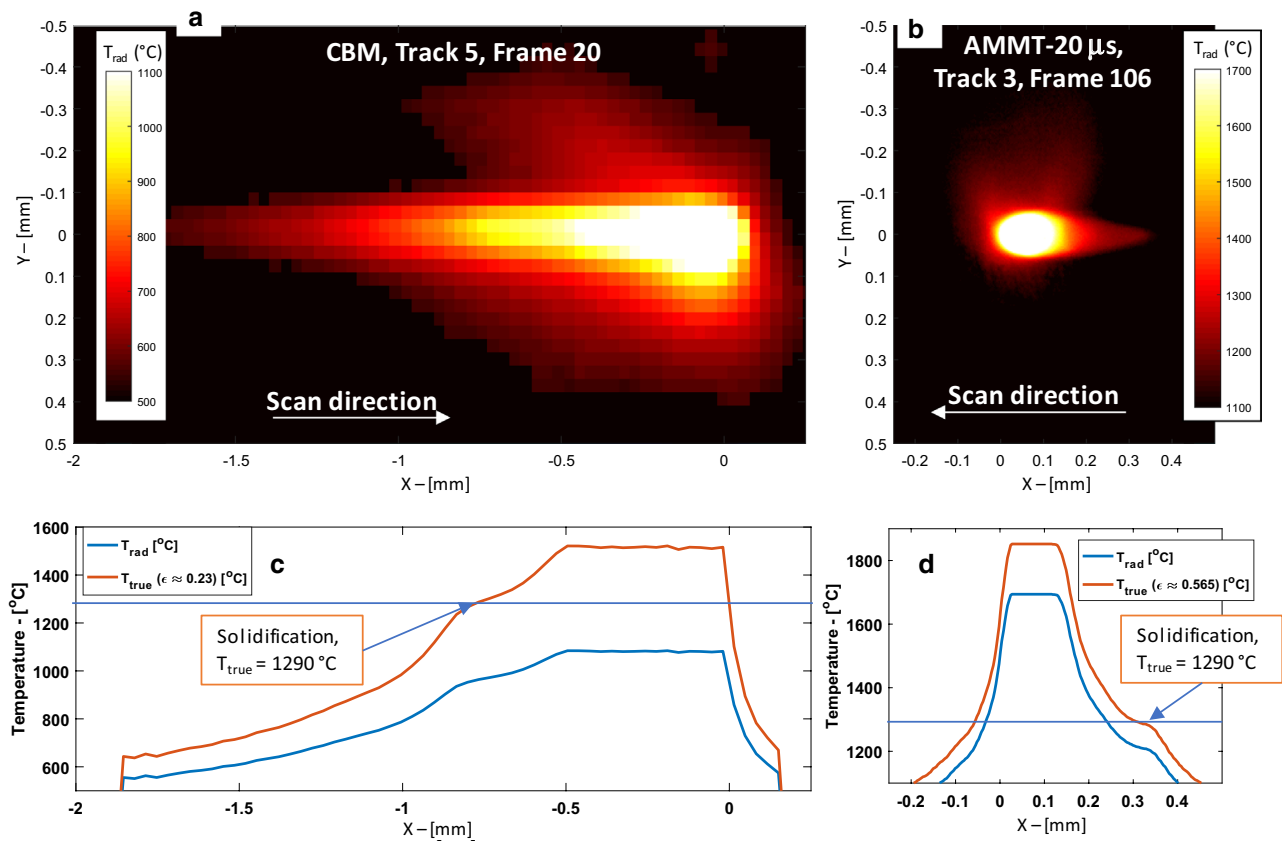
Fig. 5 Example radiance temperature thermal video frames for **a** CBM and **b** AMMT-20 μs. Example temperature profiles for, **c** CBM, **d** AMMT-20 μs

profile data. Steps 1–4 describe the method for identifying the estimated melt pool boundary and extraction of the length profile line $T(x)$ for melt pools that are not horizontally aligned in the thermographic image. Steps 5–9 use the $T(x)$ to calculate the melt pool length and cooling rate:

1. Determine the *approximate solidification* point by selecting a line of pixels (horizontal, diagonal, or otherwise) along the approximate centerline of the melt pool, creating a profile line, and locating the solidification inflection point (in $S(x)$) on the profile line determined by minimum the second derivative.
2. Calculate the solidification *approximate emittance* using the assumed freezing temperature (1290 °C for IN625) and Eq. (4).
3. Find the approximate *melt pool shape* by thresholding (binarizing) the image to values within ± 5 DL of the approximate solidification point.
4. For this binarized melt pool shape, calculate the centroid and major and minor axis orientations based on the shape central moments.

5. Use the major axis to define the melt pool *profile line* (signal vs. *x*, or $S(x)$)
6. Convert the profile line signal values to *radiance temperature* versus x ($T_{\text{rad}}(x)$) using Eq. (1).
7. Determine the solidification point T_{freeze} using the minimum of the second derivative of $T_{\text{rad}}(x)$.
8. Determine effective emittance of this point, $\varepsilon_{\text{freeze}}$, from Eq. (4), and the true temperature profile $T_{\text{true}}(x)$ from the right hand side of Eq. (1).
9. Calculate the front of the melt pool as the intersection of $x_{\text{front}} = T^{-1}(T_{\text{freeze}})$ and the lower cooling rate point $x_{\text{low}} = T^{-1}(T_{\text{low}})$, from the true temperature profile $T_{\text{true}}(x)$.

Figure 5 demonstrates an example measurement of one video frame from the CBM and AMMT-20 μs measurements, respectively. Note that although the color bars and resultant radiance temperature make the CBM melt pool apparently much larger than the AMMT melt pool, this is largely due to the different calibration ranges, where the CBM camera is capable of measuring and displaying lower

temperatures. Additionally, note that the calculated solidus emittance differs between the two figures. Although this calculated emittance is not a robust metrological value, it does have physical relationship to the normal spectral emittance of the metals, which are known to have higher normal spectral emittance at the near-infrared (such as the AMMT camera) compared to the short-wave infrared (such as the CBM camera) [9, 10]. However, when scaled via the calculated solidus emittance, the solidification points in the melt pool temperature profiles match the assigned solidus temperature of 1290 °C. Also note that the CBM had smaller laser spot size compared to the AMMT, therefore higher volumetric laser energy density, which can explain the greater measured melt pool length shown in Fig. 5, and measured depth described in the next section.

Melt pool length and cooling rates are calculated from the 'true' temperature profiles in the spatial domain $T_{true}(x)$. Melt pool length, L_x, is determined by locating the solidification inflection point via the minimum of the second derivative of the $T(x)$ profile line [4], resulting in the point x_{freeze}, and measuring the length to the front of the melt pool at the intersection of $T(x) = T_{freeze}$ (determined using linear interpolation between points) resulting in the point x_{front}. This provides for the length measurement L_x, where the subscript x indicates measurement in the spatial domain:

$$L_x = |x_{front} - x_{freeze}|. \tag{6}$$

Cooling rate measurements, as described in Sect. 3.1.2 of the AMB2018-02 test description website [1], are in units [°C/s] and measured as the difference between assumed solidus point ($T_{freeze} = 1290$ °C) and a selected lower temperature T_{low} and its respective spatial point x_{low}. The time-rate change is then calculated using the known constant scan speed $v = \Delta x / \Delta t$.

$$\dot{T}_x = \frac{v(T_{freeze} - T_{low})}{|x_{freeze} - x_{low}|}. \tag{7}$$

A cooling rate temperature range of 1290–1190 °C was selected for the two thermal imaging systems. Due to the different calibration ranges of the CBM camera, which can measure lower temperatures, broader range of 1290–1000 °C is also provided for comparison.

It should also be mentioned that that the location of the solidification point, based on the 2nd derivative of $T(x)$, minimally differs between the T_{rad} and T_{true} curves in Fig. 5, indicating that the accuracy of the assumption in $T_{freeze} = 1290$ °C has minimal effect on the length measurement. However, it can also be seen in Fig. 5 that the slopes of the $T_{true}(x)$ and $T_{rad}(x)$ profiles do differ. This indicates that the cooling rate measurement depends on the scaling from $T_{rad}(x)$ to $T_{true}(x)$, which in turn depends on T_{freeze} and

the assumption that it is applicable at temperatures below the solidification point. Additionally, T_{freeze} depends on the assumed value of $T_{freeze} = 1290$ °C. For these and other reasons, cooling rate measurements are only provided for comparison, but not recommended for reference or calibration of AM models, as described in "Results" section.

Melt Pool Transverse Cross Section Measurements

Each of the three samples in Fig. 2 was cross-sectioned through the middle of the laser traces, mounted, and polished using typical metallurgical sample preparation procedures. The samples were etched with aqua regia for 2–30 s and then examined and photographed with a Zeiss LSM800[1] confocal laser scanning microscope. The measurement mode of the microscope software was used to draw a bounding rectangle at the melt pool depth and width boundaries.

The measurement results for melt pool width and depth presented on the AM-Bench measurement results website were made from the AMMT-100 μs sample [11]. Similar measurements were later taken on the CBM sample, as detailed here. Melt pool depth and width measurements of all 10 traces on the AMMT-100 μs sample and CBM sample were acquired using three different imaging conditions: (1) 50× objective, bright field (BF), Z-stack, (2) 50× objective, reflected light dark field mode (DF), Z-stack, and (3) 50× Objective, DF, photograph at autofocus position. An enhanced depth of focus image (EDF) was compiled from each of the image stacks (ZStk) and saved as tagged image file format (TIFF) files as well as the native file format of the microscope. Example BF, Z-stack measurements for the CBM and AMMT-100 μs samples of each scan Case (A, B, and C) are shown in Fig. 6. The AMMT cases all demonstrated conduction mode track formation. The CBM-generated tracks exhibited slight keyhole or keyhole transition shape in Cases B and C, likely due to the smaller laser spot size compared to the AMMT. Additionally, the CBM Case A cross sections showed relatively elevated humping, likely due to more dynamic fluid flow within the melt pool, and again caused by the smaller laser spot size and increased laser energy density.

Melt pool cross section geometry results were later obtained for the AMMT-20 μs samples, although they utilized only one imaging technique. These were all measured using 50× objective, reflected light bright field mode, although images were collected with a 3 pixel × 3 pixel binning mode, which resulted in image scaling per pixel of 0.186 μm.
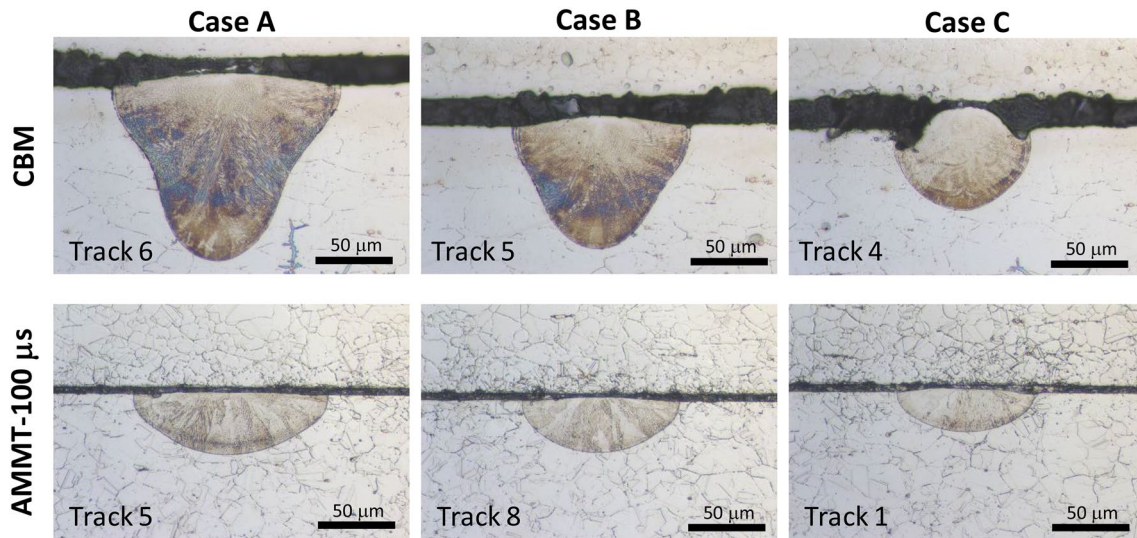
Fig. 6 Example bright field, ×50, Z-stack melt pool cross section on the CBM and AMMT-100 μs representing Cases A, B, and C. Original images are 263 μm × 176 μm, and 0.062 μm per pixel

Results

Table 3 provides a compilation of process parameters and measurement results for each scan track of each sample in Fig. 2. For thermography-based measurements (effective emittance, melt pool length, and cooling rate), the sample population N is the number of video frames in Table 3. For microscopy-based measurements (cross section width and depth), this is the number of measurements per track ($N=3$). The $\pm 1\sigma$ indicated is the standard deviation of the measurements for each individual track, whether it is number of video frames or number of microscopy measurements. Note that this does not imply a standard uncertainty, but an indication of the variance about the average values presented. These individual track measurements are compiled into a summary, later in this section in Table 4.

Melt pool cross section geometry measurements, topography, grain shapes, dendritic microstructure, etc. presented elsewhere in this special issue [12–14] were all made on the AMMT-100 μs tracks listed in Table 3. To ensure the physical scan tracks for the AMMT-20 μs and AMMT-100 μs cases were created under the same conditions (namely, laser power, scan speed, and laser spot size), melt pool cross section geometry for these two samples is compared in Fig. 7. The similar resultant cross section geometry indicates these were indeed created under the same conditions.

Since scan conditions were similar for the AMMT-100 μs and AMMT-20 μs cases, melt pool depth and width measurements made from cross section microscopy could be combined for these two datasets. The melt pool geometry measurement results are compiled to give unified reference values for each scan condition case (A, B, C), and each

machine (CBM or AMMT) and are presented in Table 4 and plotted in Fig. 8.

Since the values in Table 4 are based on mean values, it also provides the uncertainty of the mean, u_{mean}. The sample population (N) for melt pool length measurements was based on the total number of thermal video frames of all videos taken for that class. Similarly, the class mean for melt pool length defined as the average of all combined video frames for that class (e.g., the class mean for CBM Case A lengths is the average of $N=53+27+49$ total measurements) and standard uncertainty of the mean taken as $u_{mean}=\sigma/\sqrt{(N)}$. For any measurements where $N<30$, $u_{mean}=z\cdot\sigma/\sqrt{(N)}$, where z is taken from the student's t table for a confidence interval of 68.3%. Error bars in Fig. 8 represent $\pm u_{mean}$.

Melt pool cooling rate measurements were significantly different for the CBM and AMMT cases, although the trends comparing the A, B, and C cases were similar for both machines. For the AMMT-100 μs cases, the measurements at the lower temperature point, T_{low} in Eq. (6), are likely affected by motion blur from the longer 100 μs integration time. The effect of this motion blur on the temperature profile $T(x)$ is not as simple as calculating a blur length based on integration time and scan speed, $\Delta x_{blur}=(100\ \mu s)\cdot v$. This has a minimal effect on the melt pool length measurement, but does affect T_{low}; therefore, cooling rate values for the AMMT-100 μs cases should not be referred to and are noted as such in Table 3. In addition, the limited calibration range of the AMMT-20 μs measurements may have resulted in the lower temperature point, T_{low}, occurring where the calibration curve in Fig. 4 is insensitive and may be affected by sensor nonlinearity. For these reasons, cooling

Table 3 Test conditions and melt pool measurement results for CBM and AMMT cases A, B, and C used for AM-Bench reference values

Machine	Track #	Case	Power (W)	Speed (mm/s)	Laser spot diameter (µm)	# Video frames	Int. time (µm)	Effective emittance		Melt pool length (µm)		Cooling rate 1290–1190°C (°C/s)		Cooling rate from 1290 to 1000°C (°C/s)		Cross section width (µm)		Cross section depth (µm)	
								Mean	σ	Mean	σ	Mean	σ	Mean	σ	Mean	σ	Mean	σ
CBM	3	A	150	400	100	53	40	0.225	0.011	654	34	6.21E+05	7.19E+04	5.59E+05	4.46E+04	173.82	0.35	154.40	0.58
CBM	6	A	150	400	100	27	40	0.237	0.010	660	12	6.58E+05	9.41E+04	5.84E+05	5.96E+04	168.94	0.21	129.77	0.80
CBM	9	A	150	400	100	49	40	0.232	0.009	664	15	5.81E+05	4.38E+04	5.35E+05	2.55E+04	170.24	2.25	170.41	2.41
CBM	2	B	195	800	100	25	40	0.205	0.012	778	25	9.00E+05	1.65E+05	9.33E+05	9.24E+04	134.96	0.20	89.50	0.17
CBM	5	B	195	800	100	25	40	0.230	0.013	781	23	9.51E+05	1.44E+05	9.57E+05	8.16E+04	132.16	0.34	91.13	0.38
CBM	8	B	195	800	100	9	40	0.229	0.009	786	14	9.53E+05	1.11E+05	9.57E+05	7.74E+04	131.94	0.08	93.13	0.35
CBM	1	C	195	1200	100	11	40	0.169	0.020	756	56	1.31E+06	4.71E+05	1.38E+06	3.21E+05	97.82	0.20	59.61	0.39
CBM	4	C	195	1200	100	13	40	0.204	0.015	747	36	1.17E+06	3.71E+05	1.43E+06	2.46E+05	102.04	0.46	60.75	0.52
CBM	7	C	195	1200	100	15	40	0.220	0.018	758	44	1.40E+06	3.71E+05	1.54E+06	3.23E+05	100.73	0.16	60.03	0.35
CBM	10	C	195	1200	100	13	40	0.194	0.024	754	46	1.25E+06	3.13E+05	1.34E+06	2.42E+05	99.68	0.38	60.33	0.35
AMMT	5	A	137.9	400	170	51	100	0.673	0.034	350	8	1.20E+07[c]	5.66E+05	[b]	[b]	144.00	0.32	44.40	0.12
AMMT	6	A	137.9	400	170	55	100	0.667	0.044	349	9	1.45E+07[c]	4.77E+06	[b]	[b]	151.30	0.07	41.00	0.19
AMMT	7	A	137.9	400	170	55	100	0.679	0.060	346	9	1.21E+07[c]	7.15E+05	[b]	[b]	148.50	0.36	42.10	0.11
AMMT	8	B	179.2	800	170	27	100	0.575	0.065	438	12	1.97E+07[c]	1.27E+06	[b]	[b]	116.40	0.19	38.20	0.18
AMMT	9	B	179.2	800	170	31	100	0.581	0.062	421	13	1.98E+07[c]	1.82E+06	[b]	[b]	129.10	0.14	34.80	0.04
AMMT	10	B	179.2	800	170	31	100	0.583	0.032	415	10	1.90E+07[c]	1.85E+06	[b]	[b]	124.90	0.20	34.90	0.15
AMMT	1	C	179.2	1200	170	21	100	0.519	[a]	444	13	2.90E+07[c]	5.33E+06	[b]	[b]	104.40	0.19	29.00	0.08
AMMT	2	C	179.2	1200	170	22	100	0.519	[a]	435	16	2.78E+07[c]	4.88E+06	[b]	[b]	107.70	0.19	29.20	0.04
AMMT	3	C	179.2	1200	170	22	100	0.519	[a]	445	14	2.76E+07[c]	5.80E+06	[b]	[b]	106.60	0.07	30.00	0.00
AMMT	4	C	179.2	1200	170	16	100	0.519	[a]	455	11	2.83E+07[c]	4.46E+06	[b]	[b]	105.40	0.22	30.20	0.15
AMMT	2	A	137.9	400	170	19	20	0.600	0.016	300	12	1.16E+06[c]	2.68E+05	[b]	[b]	152.00	2.00	43.00	0.90
AMMT	3	B	179.2	800	170	10	20	0.565	0.017	359	20	1.08E+06[c]	5.88E+05	[b]	[b]	132.00	2.00	36.00	0.90
AMMT	1	C	179.2	1200	170	7	20	0.519	0.031	370	10	1.90E+06[c]	5.52E+05	[b]	[b]	113.00	1.00	29.00	0.90

[a] Solidus could not be detected on these samples. An assumed emittance of 0.519 based on the equivalent AMMT-20 ms measurement is used

[b] Due to limited calibration range of camera on AMMT, temperatures below 1100 °C were too erroneous to use in cooling rate measurements

[c] Due to limited calibration range for AMMT-20 ms, and motion blur for AMMT-100 ms, cooling rate values should not be used, but are printed here for reference

Table 4 Compiled summary results for melt pool geometry and cooling rate measurements on CBM and AMMT

	Cooling rate (1290–1190 °C)			Class length			Class width			Class depth		
	Mean (°C/s)	N	u_{mean} (°C/s)	Mean (mm)	N	u_{mean} (mm)	Mean (mm)	N	u_{mean} (mm)	Mean	N	u_{mean} (mm)
AMMT-A	1.16E+06	19	6.15E+04	300	19	0.50	148	9	1.07	42	9	0.49
AMMT-B	1.08E+06	10	1.86E+05	359	10	3.69	123	9	1.87	36	9	0.56
AMMT-C	1.90E+06	7	2.09E+05	370	7	7.72	106	12	0.37	30	12	0.16
CBM-A	6.20E+05	129	6.16E+03	659	129	0.47	171	9	0.82	151	9	5.75
CBM-B	9.35E+05	59	1.82E+04	780	59	0.50	133	9	0.50	91	9	0.52
CBM-C	1.28E+06	52	5.29E+04	754	52	0.68	100	12	0.48	60	12	0.16

Note that only length and cooling rate measurements from the AMMT-20 μs measurements are included (not AMMT-100 μs). Width and depth measurements incorporate both AMMT-100 μs and AMMT-20 μs measurements

Fig. 7 Comparison of tracks made on the AMMT at different thermal camera integration times (20 μs and 100 μs). Similar results indicate the scan tracks were made under similar conditions (specifically, laser power and laser spot size)
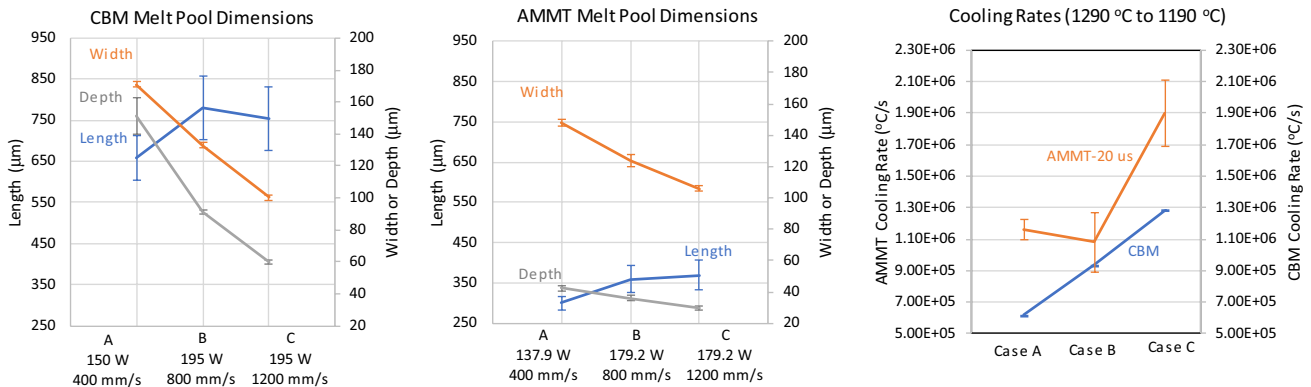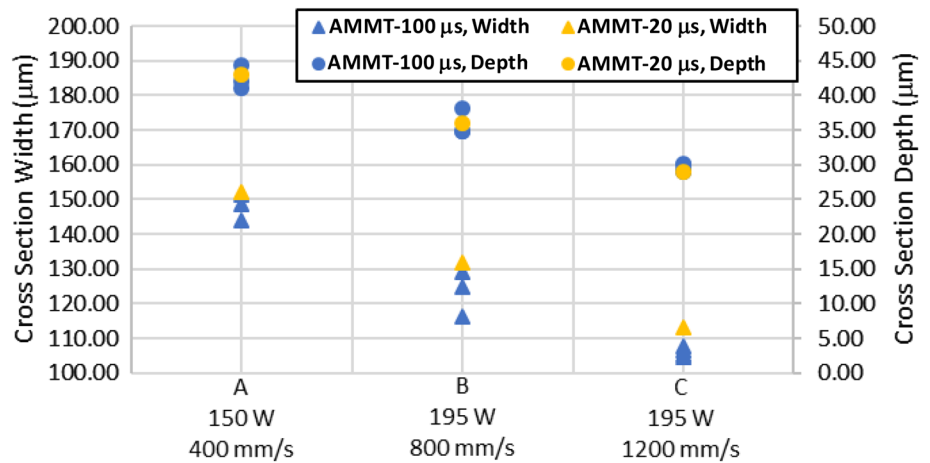

Fig. 8 Compiled summary results for melt pool geometry measurements on CBM and AMMT. Note that laser spot size was different for CBM and AMMT. Error bars indicate $\pm 1\sigma$ of the standard uncertainty of the mean, u_{mean}. A complete uncertainty analysis is provided in "Measurement Uncertainty" section

rate measurements are only given as exemplar measurement results, but not recommended for reference or calibration of AM models.

Still, the CBM and AMMT-20 μs cooling rate values cases are an order of magnitude different or more, primarily stemming from the different D4σ laser spot sizes of 100 μm and 170 μm, respectively. The melt pool lengths of the CBM sample were significantly longer than for the AMMT-20 μs sample, which coincide with the deeper melt pool depths shown in Fig. 6 and Table 4, and the longer lengths are indicative of lower cooling rates.

Table 5 Uncertainty budget for melt pool length measurements

	Unit	AMMT-100 μs			AMMT-20 μs			CBM			Prob. dist.	Analysis type
		Case A	Case B	Case C	Case A	Case B	Case C	Case A	Case B	Case C		
Components of standard uncertainty (melt pool length)												
Calibration, $u_1(T)$	[°C]	0.34	0.34	0.34	2.2	2.2	2.2	8.1	8.1	8.1	Norm.	A
Signal digitization, $u_2(S)$	[DL]	0.58	0.58	0.58	0.58	0.58	0.58	0.58	0.58	0.58	Unif.	A
Signal upsampling, $u_3(S)$	[DL]	4.62	4.62	4.62							Unif.	A
Camera signal noise, $u_4(S)$	[DL]	0.58	0.58	0.58	0.58	0.58	0.58	0.58	0.58	0.58	Unif.	A
Spatial pixelation, $u_5(x)$	[μm]	1.89	1.89	1.89	1.89	1.89	1.89	20.78	20.78	20.78	Unif.	A
Motion blur, $u_6(x)$	[μm]	23	46	69	8	16	24	16	32	48	Unif.	B
Optical blur, $u_7(x)$	[μm]	2.90	2.90	2.90	2.90	2.90	2.90	28.80	28.80	28.80	Norm.	B
Standard uncertainty of the mean, $u_8(x)$	[μm]	0.68	1.45	1.50	0.50	3.69	7.72	0.47	0.50	0.68	Norm.	A
Unit conversion factors												
Scan speed	[μm/s]	4.00E+05	8.00E+05	1.20E+06	4.00E+05	8.00E+05	1.20E+06	4.00E+05	8.00E+05	1.20E+06		
$\frac{\partial T(x_{freeze})}{\partial x}$	[°C/μm]	2.13	1.71	2.46	1.68	1.55	1.75	0.52	0.46	0.50		
$\frac{\partial F^{-1}(S_{freeze})}{\partial S}$	[°C/DL]	0.0722	0.0722	0.0722	0.3623	0.3623	0.3623	0.0268	0.0268	0.0268		
Components standard uncertainty, converted into length units [μm]												
Calibration, $u_1(x)$	[μm]	0.16	0.20	0.14	1.31	1.42	1.26	15.70	17.49	16.33		
Signal digitization, $u_2(x)$	[μm]	0.02	0.02	0.02	0.35	0.13	0.12	0.03	0.03	0.03		
Signal upsampling, $u_3(x)$	[μm]	0.16	0.19	0.14								
Camera signal noise, $u_4(x)$	[μm]	0.02	0.02	0.02	0.12	0.13	0.12	0.03	0.03	0.03		
Spatial pixelation, $u_5(x)$	[μm]	1.89	1.89	1.89	1.89	1.89	1.89	20.78	20.78	20.78		
Motion blur, $u_6(x)$	[μm]	13	27	40	5	9	14	9	18	28		
Optical blur, $u_7(x)$	[μm]	2.904	2.904	2.904	2.904	2.904	2.904	28.8	28.8	28.8		
Standard uncertainty of the mean, $u_8(x)$	[μm]	0.68	1.45	1.50	0.50	3.69	7.72	0.47	0.50	0.68		
Combined uncertainties												
Combined standard uncertainty, $u_c(x)$	[μm]	13.80	26.93	40.18	5.95	10.63	16.29	39.92	43.69	47.92		
Expanded uncertainty, U ($k=2$)	[μm]	27.59	53.86	80.36	11.91	21.26	32.57	79.84	87.39	95.85		

Measurement Uncertainty

Unit Conversions

A preliminary compilation of the components of measurement uncertainty for melt pool length is described here. Nevertheless, the following analysis and compiled uncertainty budget in Table 5 compare different factors in measurement uncertainty for the AMMT and CBM systems.

To combine the individual contributing components of measurement uncertainty, they must be converted to the same unit as the measurand (unit of length [μm] for melt pool length). Components of uncertainty given in terms of signal, $u(S)$ in units of [DL], such as digitization errors, camera noise, etc. are converted to temperature $u(T)$ in [°C] by taking the partial derivative of the inverse calibration equation $F^{-1}(S)$ from Eq. 3.

$$u(T) = \frac{\partial F^{-1}(S)}{\partial S} u(S). \tag{8}$$

The differential term is determined by partial differentiation of the inverse calibration Eq. (3), with respect to S:

$$\frac{\partial F^{-1}(S)}{\partial S} = \frac{c_2 C}{AS(C+S)\ln^2\left(\frac{C+S}{S}\right)}. \tag{9}$$

For melt pool length, this is evaluated at the solidification point. Furthermore, components of uncertainty defined in temperature units $u(T)$, such as calibration uncertainty, or those converted from signal $u(S)$, are converted to units of length $u(x)$ in [μm] utilizing reciprocal of the partial derivative of the true temperature profile $T(x)$:

$$u(x) = \left(\frac{\partial T(x)}{\partial x}\right)^{-1} u(T). \tag{10}$$

Values for dT/dx are based on the first derivative, in the spatial domain, of the true temperature profile $T(x)$, evaluated at the freezing point (e.g., d$T_{\text{true}}(x_{\text{freeze}})$/d$x$). If components of uncertainty defined in units of length are defined in pixels, these are converted to units of [μm] using the iFoV in Table 2.

Measurement Uncertainty: Melt Pool Length

Equation (6) described the measurement of melt pool length from the thermal profile $T(x)$. Since the profile line is relatively steep at the front of the melt pool (dT/dx is relatively high), the intersection of the length measurement at x_{front} is more precise than determining the location of x_{freeze}. Additionally, uncertainties in temperature $u(T)$, converted

to uncertainty in length $u(x)$ via Eq. (10), are reduced with higher dT/dx. Therefore, it is assumed that $u(x_{\text{front}}) \rightarrow 0$, and uncertainty in the melt pool length measurement is solely derived at the freezing point x_{freeze}:

$$u(L_x) = u(x_{\text{freeze}}). \tag{11}$$

The following lists those components of uncertainty that are accounted for in the uncertainty budget. Components of uncertainty due to thermal camera calibration, $u_1(T)$, stem from the curve fit procedure (in units of °C) and defined here as the root mean square error (RMSE) of the curve fit. The calibration uncertainty for the AMMT-100 μs was 0.34 °C, for AMMT-20 μs was 2.2 °C, and for CBM was 8.1 °C.

The component of uncertainty due to signal digitization, $u_2(S)$, is assumed to be ± 1 DL with uniform probability distribution, resulting in a standard uncertainty of $1/\sqrt{3} = 0.58$ DL.

The AMMT-100 μs case was originally collected at 8-bit (256 DL) dynamic range and was upconverted to 12-bit (4096 DL) digital range, resulting in a 16x loss in precision (± 8 DL). An added component of uncertainty is provided assuming uniform probability distribution, of $u_3(S) = 8/\sqrt{3}$ [DL].

Signal noise or the temporal noise of flicker of the thermal camera pixels for both AMMT and CBM was typically ± 1 DL. Assuming uniform probability distribution results in $u_4(S) = 1/\sqrt{3} = 0.58$ DL

Uncertainty due to spatial pixilation is assumed to be ± 1 pixel, with uniform probability. This is converted to [μm] using the iFoV in Table 2, resulting in $u_5(x) = $ iFoV$/\sqrt{3}$ μm.

Motion blur and optical blur are mathematically complicated, and their incorporation into measurement uncertainty in thermal or other imaging-based metrology is not standardized. Optical blur stems from the inherent resolution limits of optical system, which depend on many factors, but primarily depend on the measured wavelength and numerical aperture (i.e., the Airy disk diameter or diffraction limit [15]). Motion blur depends on the relative speed of an object or scene with respect to the integration time or shutter speed. Mathematically, both optical blur and spatial blur affect a 'perfect' image through convolution of a 2D spatial filter. How this convolution affects the image depends on the convolution filter kernel, as well as the *specific image or scene*. In other words, the measurement uncertainty stemming from blur will depend on the 'perfect' image being measured. As yet, no closed form or simple formulation is known to exist that can be generally applied to determine the contribution of blur to a dimensional measurement on a varying set of images or video.

A conservative, Type B estimate is provided here for motion blur ($u_6(x)$) and optical blur ($u_7(x)$). Uncertainty in length measurement due to motion blur is assumed to

be equal to 2× the blur length, calculated as $\delta x = 2\ v\cdot\text{tint}$ where v is the scan speed and tint is the integration time. The measured point is assumed to exist within δx with uniform probability, resulting in $u_6(x) = v\cdot\text{tint}/\sqrt{3}$. Optical blur is estimated as $u_7(x) = 2\sigma$ width of an assumed rotationally symmetric gaussian point spread function, measured using knife edge technique described in ISO-12233 [16, 17]. Optical blur is assumed to have a normal distribution.

Standard uncertainty of the mean was described prior to Table 4. The class mean for melt pool length defined as the average of all combined video frames for that class (e.g., the class mean for CBM Case A lengths is the average of $N = 53 + 27 + 49$ total measurements), and standard uncertainty of the mean taken as $u_8(x) = \sigma/\sqrt{(N)}$. The sample population (N) for melt pool length measurements was based on the total number of thermal video frames of all videos taken for that class. For any measurements where $N < 30$, $u_8(x) = z\cdot\sigma/\sqrt{(N)}$, where z is taken from the student's t table for a confidence interval of 68.3%.

The ISO Guide to the Expression of Uncertainty in Measurement [18] gives the formula for combining uncertainties in the absence of correlations for the combined standard uncertainty, u_c. This requires that each component of uncertainty by converted to standard uncertainty with equivalent normal probability distribution. For those components that are given with a rectangular probability distribution of the range $\pm a$ (in units of that component of uncertainty), these are converted to their equivalent standard uncertainty by a factor of $2a/\sqrt{12}$ or $a/\sqrt{3}$ prior to unit conversion. Each component of standard uncertainty is converted to length units using Eqs. (8)–(10), then added in quadrature:

$$u_c^2(x) = \sum_n \left(\frac{\partial T(x)}{\partial x}\right)^{-2} u_n^2(T) + \sum_m \left(\frac{\partial T(x)}{\partial x}\right)^{-2} \left(\frac{\partial F^{-1}(S)}{\partial S}\right)^2 u_m^2(S) + \sum_l u_l^2(x). \tag{12}$$

$u_n^2(T)$ are the squares of those components defined in units of temperature [°C] ($n = 1$), $u_m^2(S)$ are the squares of those components defined in units of signal [DL] ($m = 2$ to 4), and $u_l^2(x)$ are the squares of those components defined in units of length [μm] ($l = 5$–8).

Table 1 lists each component of standard uncertainty, the unit conversion factors, and the components converted to length units. Finally, the combined standard uncertainty is provided calculated using Eq. (12) and expanded uncertainty assuming coverage factor $k = 2$ [19].

Some components of uncertainty are assumed negligible. Variability in scan speed and resulting effects are neglected. The high speed cameras have very precise timing clocks (> 1 MHz) and precise frame rates. Cursory observation of the transit of the melt pool across image frames for both the CBM and AMMT cameras demonstrated that the scan speed, measured as the distance moved between frames divided by

frame period, resulted in variability far less than one pixel width. Variability in integration time and resulting effects on measurement is similarly neglected due to the precise timing of the camera clocks.

Measurement Uncertainty: Cross Section Width and Depth

Uncertainty due to optical resolution limits in the microscope images is accounted for based on the Rayleigh criterion and illumination wavelength of the microscope. This was estimated to be 0.5 μm (Type B).

Uncertainty due to variability along the track stems from the fact that these measurements are based on a subset of transverse metallographic cross sections, whereas the actual geometries of the track can vary in the longitudinal direction. This effect is minimized when performing laser scans on relatively smooth, bare metal surfaces when compared to single layers of metal powder. Ricker et al. [13] provide topological measurements in the longitudinal direction of the tracks. However, melt pool width or depth was not measured along the longitudinal direction. For width, Fox et al. [20] measured variability along a track width on a 17–4 stainless steel plate, resulting in a 1σ variation of 1.8%. This was conducted on 'as-received' surface, which is rougher than those used in this paper, likely contributing to a relatively more variation in track width. Based on this, a conservative estimate of 2% uncertainty in variability track width is accounted for (Type B).

Similarly, variability in track depth is not measured since longitudinal cross sections along the track length were not obtained. However, the authors believe this effect to vary less than 5%, with greatest variation for CBM track A since the cross sections in Fig. 6 demonstrate it to have occurred near or at keyholing regime. King et al. [21] created longitudinal cross sections and noted a 15% variability in depth along 316L stainless steel scan tracks. However, an example track in King et al. had significantly higher volumetric energy density, defined as $E = P/V/A$ [J/mm^3], where P is laser power [W], V is scan speed [mm/s], and A is the area of the laser spot based on D4σ diameter [mm^2]. This indicates that King et al. utilized $E = 124$ J/mm^3, whereas CBM Case A utilized 48 J/mm^3. Although track depth fluctuations likely do not scale directly with energy density, and materials in AM-Bench and King et al. were different, this indicates track depth variability for CBM case A is likely much less than 15% in [21]. Conservative estimates of 5% of mean depth are assumed for all AMMT and CBM cases (Type B).

Table 6 Uncertainty budget for the melt pool width for the AMMT and CBM cases compiled in Table 4

	Unit	AMMT			CBM			Prob. dist.	Analysis type
		Case A	Case B	Case C	Case A	Case B	Case C		
Components of standard uncertainty (melt pool width)									
Optical resolution	[μm]	0.50	0.50	0.50	0.50	0.50	0.50	Norm.	B
Variability along track	[μm]	2.96	2.46	2.12	3.42	2.66	2.00	Norm.	B
User selection	[μm]	0.37	0.37	0.37	0.37	0.37	0.37	Norm.	A
Standard uncertainty of the mean	[μm]	1.07	1.87	0.37	0.82	0.50	0.48	Norm.	A
Combined uncertainties									
Combined standard uncertainty, u_c	[μm]	3.21	3.15	2.24	3.57	2.78	2.15		
Expanded uncertainty, U ($k=2$)	[μm]	6.42	6.30	4.48	7.14	5.56	4.30		

Table 7 Uncertainty budget for the melt pool depth for the AMMT and CBM cases compiled in Table 4

	Unit	AMMT			CBM			Prob. dist.	Analysis type
		Case A	Case B	Case C	Case A	Case B	Case C		
Components of standard uncertainty (melt pool width)									
Optical resolution	[μm]	0.50	0.50	0.50	0.50	0.50	0.50	Norm.	B
Variability along track	[μm]	2.10	1.80	1.50	7.55	4.55	3.00	Norm.	B
User selection	[μm]	0.37	0.37	0.37	0.37	0.37	0.37	Norm.	A
Standard uncertainty of the mean	[μm]	0.49	0.56	0.16	5.75	0.52	0.16	Norm.	A
Combined uncertainties									
Combined standard uncertainty, u_c	[μm]	2.25	1.99	1.63	9.51	4.62	3.07		
Expanded uncertainty, U ($k=2$)	[μm]	4.49	3.97	3.26	19.02	9.24	6.14		

User variability in the track boundary selection in the microscopic images had an approximate ± 6 pixel repeatability for the 0.062 μm/pixel resolution images, and ± 2 pixel repeatability for the 0.186 μm/pixel images, resulting in user variability uncertainty of ± 0.372 μm (Type A) for all measurements.

The total number of measurements, N, and the experimental standard uncertainty of the mean, u_{mean}, are provided in Table 4. Since the number of measurements made of the microscope images was $N < 30$, u_{mean} is scaled based on Student t distribution to represent a 68.3% (1σ) confidence interval as described in the text prior to Table 4.

Since each component of uncertainty is already defined in units of length, no unit conversions are necessary, and the combined standard uncertainty of the width $u_c(w)$ or length $u_c(d)$, without correlations, is given as the sum of uncertainty components in quadrature:

$$u_c^2(w) = \sum_i u_i^2(w).$$

(13)

Expanded uncertainty, U, utilizes coverage factor $k = 2$ [19]. Tables 6 and 7 provide the uncertainty budgets for melt pool width and depth, respectively.

Discussion and Conclusions

This paper described the experiment setup and measurement results for the AMB2018-02 measurement challenges for melt pool geometry. These experiments consisted of LPBF tracks scanned on bare IN625 plates, in situ melt pool length and cooling rate measurements via thermography and ex situ transverse cross section geometry (width and depth) via optical microscopy. A summary of compiled results is provided in Table 4, and preliminary measurement uncertainty analysis is provided in Tables 5, 6 and 7. Cooling rates are provided, but to be considered as exemplar data, but not reference data.

Melt pool cross section measurements, such as width and depth, as well as microstructural measurements (grain shapes and dendritic microstructure) provided for the 2018 AM-Bench challenges [1] were from the AMMT-100 μs tracks given in Table 4 [12, 13]. However, due to motion blur in the thermographic system, melt pool length measurements should be taken from AMMT-20 μs tracks or the CBM tracks. It was found that cooling rate measurements were significantly different for the AMMT and CBM systems, likely stemming from differences in the imaging systems that affect temperature values much below the solidification point. It

was shown in Fig. 7 that the AMMT-100 µs and AMMT-20 µs tracks were fabricated under comparable conditions (laser power, scan speed, and laser spot size).

Melt pool length measurements using thermography have larger uncertainty than cross section width or depth measurements taken via optical microscopy, primarily due to differences in spatial resolution. However, with thermography, greater number of measurements or image frames can be taken, which can elucidate transient variations. Variability in melt pool depth along the track is based on review of external publication [21] and likely depends on the melt pool formation mode (conduction or keyhole).

Further work is necessary to better identify this variability, potentially with new methods for longitudinal track cross sections, and how the measured variability may contribute to melt pool depth measurement uncertainty from more easily obtained transverse cross sections.

References

1. Liepa T, AMB2018-02 Description, NIST (2018). https://www.nist.gov/ambench/amb2018-02-description. Accessed 15 Feb 2019
2. Heigel JC, Lane BM (2017) The effect of powder on cooling rate and melt pool length measurements using in situ thermographic techniques. In: Proceedings of the solid freeform fabrication symposium, Austin, TX, pp 1340–1348
3. Lane B, Mekhontsev S, Grantham S, Vlasea M, Whiting J, Yeung H, Fox J, Zarobila C, Neira J, McGlauflin M, Hanssen L, Moylan S, Donmez MA, Rice J (2016) Design, developments, and results from the NIST additive manufacturing metrology testbed (AMMT). In: Proceedings of the 26th annual international solid freeform fabrication symposium, Austin, TX, pp 1145–1160
4. Heigel J, Lane B (2017) Measurement of the melt pool length during single scan tracks in a commercial laser powder bed fusion process. In: Proceedings of the international conference on manufacturing science and engineering, Los Angeles, CA, 2017
5. Lane B, Moylan S, Whitenton EP, Ma L (2016) Thermographic measurements of the commercial laser powder bed fusion process at NIST. Rapid Prototyp J 22:778–787
6. Sakuma F, Hattori S (1982) Establishing a practical temperature standard by using a narrow-band radiation thermometer with a silicon detector. In: Temperature, its measurement and control in science and industry. AIP, New York, pp 421–427
7. Woolliams ER, Anhalt K, Ballico M, Bloembergen P, Bourson F, Briaudeau S, Campos J, Cox MG, del Campo D, Dong W, Dury MR, Gavrilov V, Grigoryeva I, Hernanz ML, Jahan F, Khlevnoy B, Khromchenko V, Lowe DH, Lu X, Machin G, Mantilla JM, Martin MJ, McEvoy HC, Rougié B, Sadli M, Salim SGR, Sasajima N, Taubert DR, Todd ADW, Van den Bossche R, van der Ham E, Wang T, Whittam A, Wilthan B, Woods DJ, Woodward JT, Yamada Y, Yamaguchi Y, Yoon HW, Yuan Z (2016) Thermodynamic temperature assignment to the point of inflection of the melting curve of high-temperature fixed points. Philos Trans R Soc Math Phys Eng Sci 374:20150044. https://doi.org/10.1098/rsta.2015.0044
8. Ghosh S, Ma L, Levine LE, Ricker RE, Stoudt MR, Heigel JC, Guyer JE (2018) Single-track melt-pool measurements and microstructures in Inconel 625. JOM 70:1011–1016. https://doi.org/10.1007/s11837-018-2771-x
9. del Campo L, Pérez-Sáez RB, González-Fernández L, Esquisabel X, Fernández I, González-Martín P, Tello MJ (2010) Emissivity measurements on aeronautical alloys. J Alloys Compd 489:482–487. https://doi.org/10.1016/j.jallcom.2009.09.091
10. Teodorescu G, Jones PD, Overfelt RA, Guo B (2008) Normal emissivity of high-purity nickel at temperatures between 1440 and 1605 K. J Phys Chem Solids 69:133–138. https://doi.org/10.1016/j.jpcs.2007.08.047
11. Liepa T, CHAL-AMB2018-02-MP-xsection, NIST. (2018). https://www.nist.gov/ambench/chal-amb2018-02-mp-xsection. Accessed 15 Feb 2019
12. Stoudt M, Williams ME, Levine LE, Creuziger AA, Young SW, Heigel JC, Lane BM, Phan TQ (2020) Location-specific microstructure characterization within In625 additive manufacturing benchmark test artifacts. Integr Mater Manuf Innov
13. Ricker RE, Heigel JC, Lane BM, Zhirnov I, Levine LE (2019) Topographic measurement of individual laser tracks in alloy 625 bare plates. Integr Mater Manuf Innov. https://doi.org/10.1007/s40192-019-00157-0
14. Levine LE, Lane BM, Heigel JC, Migler K, Stoudt MR, Phan TQ, Ricker RE, Strantza M, Hill MR, Zhang F, Seppala J, Garboczi E, Bain E, Cole D, Allen AJ, Fox JC, Campbell C (2020) Outcomes and conclusions from the 2018 AM-Bench measurements, challenge problems, modeling submissions, and conference. Integr Mater Manuf Innov. https://doi.org/10.1007/s40192-019-00164-1
15. Holst GC (2008) Testing and evaluation of infrared imaging systems. SPIE Press, Bellingham
16. ISO 12233:2014, Photography—electronic still-picture cameras—resolution measurements, ISO, Geneva, Switzerland, n.d
17. Lane B, Whitenton E (2015) Calibration and measurement procedures for a high magnification thermal camera. National Institute of Standards and Technology, Gaithersburg
18. I. BIPM IFCC, ISO, IUPAC, IUPAP., Guide to the Expression of Uncertainty in Measurement (GUM), International Organization for Standardization Geneva (1995)
19. Taylor BN, Kuyatt CE (1994) Guidelines for evaluating and expressing the uncertainty of NIST measurement results. NIST Technical Note 1297. https://doi.org/10.6028/NIST.TN.1297
20. Fox JC, Lane BM, Yeung H (2017) Measurement of process dynamics through coaxially aligned high speed near-infrared imaging in laser powder bed fusion additive manufacturing. In: Proceedings of the SPIE 10214 thermosense: thermal infrared applications, XXXIX, Anaheim, CA, pp 1021407–17. https://doi.org/10.1117/12.2263863
21. King WE, Barth HD, Castillo VM, Gallegos GF, Gibbs JW, Hahn DE, Kamath C, Rubenchik AM (2014) Observation of keyhole-mode laser melting in laser powder-bed fusion additive manufacturing. J Mater Process Technol 214:2915–2925. https://doi.org/10.1016/j.jmatprotec.2014.06.005